

**IDETC2019-98205**

## **SELF-ADAPTING INTELLIGENT BATTERY THERMAL MANAGEMENT SYSTEM VIA ARTIFICIAL NEURAL NETWORK BASED MODEL PREDICTIVE CONTROL**

**Yuanzhi Liu\***

The University of Texas at Dallas  
Richardson, TX 75080  
Email: yuanzhi.liu@utdallas.edu

**Jie Zhang†**

The University of Texas at Dallas  
Richardson, TX 75080  
Email: jiezhang@utdallas.edu

### **ABSTRACT**

*This paper develops a self-adaptive control strategy for a newly-proposed J-type air-based battery thermal management system (BTMS) for electric vehicles (EVs). The structure of the J-type BTMS is first optimized through surrogate-based optimization in conjunction with computational fluid dynamics (CFD) simulations, with the aim of minimizing temperature rise and maximizing temperature uniformity. Based on the optimized J-type BTMS, an artificial neural network (ANN)-based model predictive control (MPC) strategy is set up to perform real-time control of mass flow rate and BTMS mode switch among J-, Z-, and U-mode. The ANN-based MCP strategy is tested with the Urban Dynamometer Driving Schedule (UDDS) driving cycle. With a genetic algorithm optimizer, the control system is able to optimize the mass flow rate by considering several steps ahead. The results show that the ANN-based MPC strategy is able to constrain the battery temperature difference within a narrow range, and to satisfy light-duty daily operations like the UDDS driving cycle for EVs.*

*Keywords: Battery thermal management system, surrogate-based optimization, artificial neural network, model*

*predictive control, electric vehicles*

### **1 INTRODUCTION**

Lithium-ion batteries (LIB), as the primary traction power source, have been extensively employed in electric vehicles due to its distinguished properties like high energy density, low self-discharging, and low maintenance. However, several critical issues such as gradual aging effects and narrow operating temperature range, still need to be addressed before EVs' next massive expansion. For primary LIB technologies nowadays, studies have suggested that the appropriate operating temperature should be maintained between 15°C to 45°C due to its intrinsic chemistry and thermal properties [1, 2]. Otherwise, it may trigger capacity reduction, electrode degradation, or even safety issues under extreme low-temperature and high-temperature environment [3]. Therefore, it is critically important to design and optimally control a battery thermal management system (BTMS) with high efficiency.

A significant amount of research has been conducted in the literature to examine and explore the heat transfer medium coupled with its appropriate structures. State-of-the-art heat transfer mediums include air, fluid, phase change material, heat pipe, and a combination of them [4]. All the mediums other than air and fluid are still under lab experimental stage due to their complexities and instability. Air-based BTMS is currently widely applied in light-duty EVs due to its unparalleled advantages like light

---

\*Ph.D. Student, Department of Mechanical Engineering, ASME Student Member.

†Assistant Professor, Department of Mechanical Engineering, ASME Professional Member. Address all correspondence to this author.

weight, simple structure, and low cost. Although fluid-based cooling technologies are more preferred to address the newly-rising challenges like fast charging, air-based cooling technologies are still worth to be explored especially together with optimal control strategies because of its excellent performance. For instance, Nissan Leaf 2018 and Volkswagen E-Golf 2017 directly utilize passive air cooling technologies, while Renault Zoe40 2017, Chevrolet Bolt EV, and Toyota Prius Prime use active air cooling strategies. All these models have been successfully updated for several generations, showing that the air-based system is trustworthy and able to meet the market expectations [5].

Existing studies of air-based BTMS have mainly focused on battery pack structure design and optimization [6, 7]. The typical parallel-channel BTMS configuration is usually referred to as a  $U$ -type (reverse flow) or a  $Z$ -type (parallel flow) structure, depending on the air flow direction. Several modified structures have been proposed with better thermal performance, e.g., uneven battery channel interspacing size [8], tapered manifold configurations [9], and other specific manifold structures that seek to allocate the mass flow rate of each channel uniformly [10, 11]. However, the majority of these studies only optimized the geometry structures for a single stable working condition without adaptively modifying and controlling BTMS under changing working conditions. As a result, when the battery working condition changes, BTMS may fail to work as effectively as its original optimal design or lead to issues like temperature nonuniformity and inefficiency. Several studies have proposed to use classical PID and fuzzy logic systems to control the air-based BTMS at the system level. Because of the intrinsic limitations of  $U$ -type,  $Z$ -type, or other through-type structures, the thermal performance is impressive but probably far from optimum [12, 13, 14].

This paper seeks to design and adaptively control an air-based BTMS using a model predictive control (MPC) strategy coupled with a newly developed  $J$ -type BTMS structure. The  $J$ -type air-based BTMS [15] was developed by integrating the benefits of popularly used  $U$ - and  $Z$ -type structures. The main differences between the novel  $J$ -type and traditional  $U$ - and  $Z$ -type structures are: (i) there are two outlets in the  $J$ -type BTMS compared to one outlet in  $U$ - and  $Z$ -type BTMS; and (ii) two control valves are employed to adjust the openness of each outlet, increasing the flexibility of BTMS to switch from  $J$ -mode to either  $U$ -mode or  $Z$ -mode. To improve the computational efficiency, the channels in the  $J$ -type structure are arranged in multiple groups and pre-optimized using surrogate-based optimization. Then the optimized  $J$ -type BTMS will employ an MPC strategy along with three control modes, i.e.  $J$ -mode,  $U$ -mode, and  $Z$ -mode, to effectively control the battery temperature.

The remainder of the paper is organized as follows. First, a lithium-ion battery electro-thermal model is developed. Then, the optimization of grouped-channel  $J$ -type BTMS is conducted to uniform the battery pack temperature distribution under a benchmark working condition. Thirdly, an artificial neural network (ANN)-based MPC strategy is constructed by considering an urban dynamic driving cycle. Concluding remarks and future work are discussed in the last section.

## 2 BATTERY ELECTRO-THERMAL AND BTMS MODELING

### 2.1 Battery Electro-thermal Model

Extensive studies have indicated that the volumetric heat generation rate of LIB is strongly affected by the charging/discharging current, operating temperature, state of charge (SoC), and cycles [16]. A simplified LIB heat generation model can be expressed as Eq. 1 [17].

$$\dot{Q} = I(V - V_{oc}) + IT \frac{\partial V_{oc}}{\partial T} \quad (1)$$

where  $\dot{Q}$  represents the battery heat generation rate,  $V$  and  $V_{oc}$  denote the open circuit voltage and the cell voltage, respectively.  $T$  is the battery cell operation average temperature,  $\partial V_{oc}/\partial T$  is named as the entropic heat coefficient, and  $I$  is the charging or discharging current.

For simplification, the heat source in Eq. 1 is assumed to be uniform and homogeneous, the radiation heat transfer is neglected here, and the battery thermal behavior can be estimated using the lumped thermal model, as shown in Eq. 2.

$$mC_p \frac{\partial T}{\partial t} = \dot{Q} - hA(T_{cell} - T_{\infty}) \quad (2)$$

where  $m$  denotes the mass of a battery cell,  $C_p$  is the average heat capacity,  $h$  represents the convective heat transfer coefficient,  $A$  is the effective surface area, and  $T_{\infty}$  is the free stream temperature of the cooling media.

### 2.2 Battery Equivalent Circuit Model

For the LIB equivalent electric circuit model, several hypotheses have been proposed to characterize the relationships between battery electrical characteristics and its thermal behavior. The first order equivalent circuit is broadly used for traction power source integration, as shown in Fig. 1. The electric model consists of an ideal voltage source, an internal ohmic resistance, and a parallel RC circuit. The RC

circuit is utilized here to interpret the dynamic responses. All the parameters are contingent on the SoC, operation temperature, and battery cycle. The mathematical expression of the equivalent circuit is derived and given by:

$$V_t = V_{oc} - I \cdot R_D - I \cdot R_o + (I \cdot R_D)e^{-\frac{t-t_0}{\tau}} \quad (3)$$

where  $I \cdot R_D$  is the potential drop on  $RC$  circuit,  $I \cdot R_o$  is the potential drop on the internal resistance, and  $\tau = R_D \cdot C_D$  denotes the time constant.

These parameters in Eq. 3 can be measured using the method of hybrid pulse power characterization (HPPC) test. In this study, graphite/ $LiMn_2O_4$  pouch battery cells with a capacity of 1.6 Ah, and a nominal voltage of 3.75 V are used for experiments. The heat generated by the resistances  $R_o$  and  $R_D$  is considered equal to the internal heat source. The details of experiment setup, parameters analyses, and results validations can be found in Refs. [18, 19]. The extracted data, i.e., current, SoC, and operating temperature, is then utilized to construct the battery thermal model.

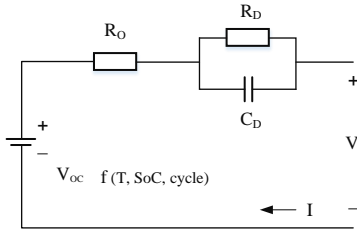


FIGURE 1: First order equivalent circuit model for LIB

### 2.3 Visualization of Battery Electro-thermal Model

After cross-validation, a Kriging approximation with the second order polynomial regression and exponential error estimation is utilized here to create a battery electro-thermal model based on the experimental data. The model inputs consist of the battery current, SoC, and operating temperature; the model output is the volumetric heat generation rate. The deterministic response  $\mathcal{G}(I, SoC, T)$  with three features is formulated as follows:

$$\mathcal{G}(I, SoC, T) = \mathcal{F}(\lambda, I, SoC, T) + \mathcal{R}(\omega, I, SoC, T) \quad (4)$$

where  $\mathcal{F}$  is defined as the regression model, and  $\mathcal{R}$  is the approximation error. All the Kriging parameters  $\lambda, \omega$  are solved by using the generalized least squares estimation method [20].

Figure 2 shows the equivalent volumetric heat generation rate distribution with respect to the operation current,

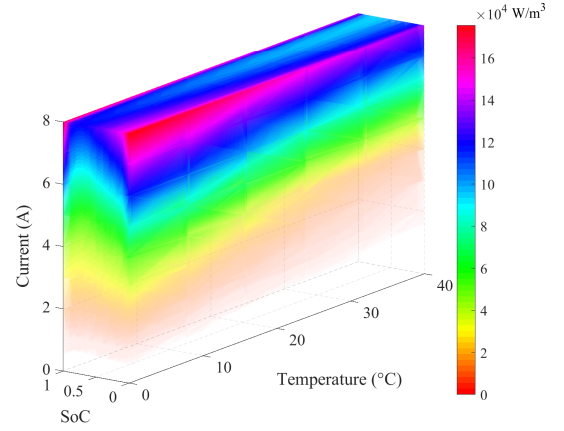


FIGURE 2: The equivalent volumetric heat generation rate distribution with respect to current, SoC, and temperature

SoC, and temperature. It indicates that the internal resistance decreases as the operation temperature increases. This is due to the increased electron mobility and reaction rate at higher temperatures, which will increase heat generation rate. The calorific value is relatively low around 60% SoC, which has also been reported in the literature [16]. Additionally, the overall battery thermal performance is more sensitive to the operating current than other parameters.

### 2.4 CFD Modeling of J-type BTMS

Ideally, the valve opening of the two control valves on the outlets is expected to be adaptively controlled according to the battery working conditions. However, a large number of simulations are needed to prepare the raw data under various working conditions. So only three modes are considered in this paper for the sake of simplification, which are the  $J$ -mode,  $Z$ -mode, and  $U$ -mode, as presented in Fig. 3. The BTMS prototype consists of ten battery cells, with a geometry size of 151 mm in height, 65 mm in length, and 16 mm in width.

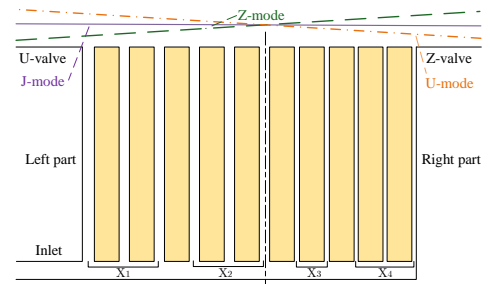
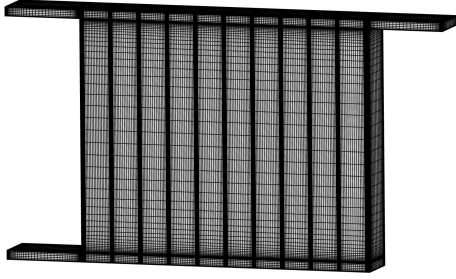


FIGURE 3: Schematic diagram of a  $J$ -type air-based BTMS

Figure 4 shows the CFD meshing settings of the  $J$ -type BTMS. The total mesh size converges to 1,700,000 ele-



**FIGURE 4:** The 3D mesh setting of J-type CFD model

ments after grid independence analysis. The inlet and outlet boundary conditions are mass flow rate inlet and pressure outlet, respectively. Radiative heat transfer is neglected because the temperature difference is small. The battery cell is considered to be homogeneous with a uniform heat source.

### 3 SURROGATE-BASED OPTIMIZATION OF J-TYPE BTMS

Our previous studies have found that the BTMS structure, channel interspacing size in particular, have remarkable influence on the system performance [10]. In this study, surrogate-based optimization is employed to minimize the maximum temperature of battery cells by optimizing the interspacing sizes of grouped-channels. With the optimal structure, BTMS can adaptively adjust the opening degree of the two valves in the J-type structure and the air mass flow rate, seeking to uniformize the temperature among all battery cells.

#### 3.1 Surrogate Model Selection

The Latin hypercube method is employed to perform a design of experiments (DoE). The four grouped-channel interspacing sizes are chosen as the design variables, as illustrated in Fig. 3. All CFD simulations are conducted under the predefined benchmark working condition, in which the mass flow rate is set as  $7.1 \text{ g/s}$ , and the equivalent heat source is approximately  $33,800 \text{ W/m}^3$ . The heat source is defined by the battery electro-thermal model under the benchmark electric condition of 3 C-rate discharging current, 1 SoC, and  $300 \text{ K}$  environment temperature, and is hooked into Fluent simulations using a user-defined function. A total of 50 simulations are conducted, 75% of which are utilized as training data, and the rest are treated as test data.

An ensemble surrogate model is developed for BTMS modeling. A large pool of surrogate models are first constructed, which consists of five major groups of surrogate models and there are 62 submodels in total regarding dif-

ferent kernel functions or hyper parameters, e.g., Artificial Neural Network (ANN), Kriging/Gaussian Process Regression (GPR), Support Vector Machine (SVM), Radial Basis Functions (RBF), and Polynomial Response Surface (PRS). During the ensemble member model selection and training process, a weighted evaluating criterion is employed here to determine the appropriate models after K-fold cross-validation. Adopted criteria include the normalized maximum absolute error (NMAE) and normalized root mean square error (NRMSE), as given by:

$$NMAE = \frac{1}{n} \sum_{k=1}^n \left| \frac{\hat{y}_k - y_k}{y_{max} - y_{min}} \right| \quad (5)$$

$$NRMSE = \frac{1}{y_{max} - y_{min}} \sqrt{\frac{\sum_{k=1}^n (\hat{y}_k - y_k)^2}{n}} \quad (6)$$

where  $\hat{y}$ ,  $y$ ,  $y_{max}$  and  $y_{min}$  denote the corresponding estimated value, actual value, maximum value, and minimum value, respectively.  $n$  is the number of test data used in evaluation.

Table 1 summarizes the top 6 surrogate models selected from the cross-validation evaluation. These six submodels are integrated together by using the weights calculation method from the Extensive Adaptive Hybrid Function (EAHF) [21, 22].

**TABLE 1:** The top 6 surrogate models selected from the cross-validation evaluation

Model-Kernel	NMAE	NRMSE
GPR-Ardmatern32	<b>3.97</b>	<b>5.23</b>
GPR-Matern32	4.11	5.57
RBF-Cubic	4.14	5.40
PRS-Cubic	4.27	5.59
RBF-TPS	4.37	5.94
KRG-Poly2gauss	4.73	6.41

The estimations and errors of the ensemble surrogate model and the selected member models are shown in Fig. 5. Note that the ensemble model does not necessarily perform the best at every local estimation due to the high nonlinearity of the problem. However, the ensemble model captures the overall trend of the problem and provides the best global accuracy.

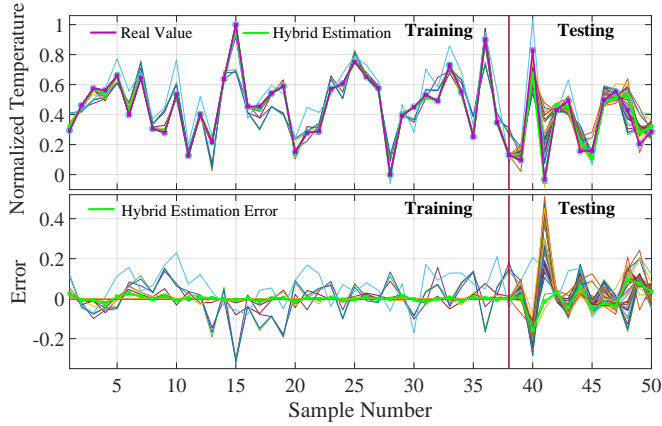


FIGURE 5: Surrogate model estimation and error

### 3.2 Surrogate-based Optimization and Resampling

The objective is to minimize the maximum temperature  $T_{max} = f(x_1, x_2, x_3, x_4)$ , and the optimization problem is formulated as:

$$\begin{aligned} \arg \min_X \quad & T_{max} = f(x_1, x_2, x_3, x_4) \\ \text{subject to} \quad & 2.0 \leq x_i \leq 5.0 \quad i = (1, 2, 3, 4) \end{aligned} \quad (7)$$

where  $x_1 - x_4$  represent the grouped interspacing size from the left side to the right side.

The genetic algorithm is adopted here to perform the surrogate-based optimization. Figure 6 shows the overall framework of surrogate-based optimization and resampling. Here, a two-stage cluster resampling method is employed, in which the first stage is to cluster the candidate optimal solutions from a surrogate model pool, and the second stage is to generate the adaptive samples using a Gaussian mixed model (GMM). The newly added samples consist of two parts: the selected optimized solutions and the samples generated by GMM. The optimization and resampling process are stopped when the convergence criterion is met, as defined by:

$$BIAS = \left| \frac{Y_k^* - Y_{k-1}^*}{Y_{k-1}^*} \right| \leq 0.001 \quad (8)$$

where  $Y_k^*$  and  $Y_{k-1}^*$  are the best optimization result of the  $k$ -th resampling and  $(k-1)$ -th resampling, respectively, and 0.001 is a predefined convergence tolerance. After two rounds of resampling, as shown in Fig. 7, the resampling results converge to a small design range, where the bias equals to  $9.3E-10^4$ . The best sample among all the resampling data is regarded as the optimal solution.

The optimal BTMS design is summarized in Table 2. Compared with the benchmark case with a uniform spacing

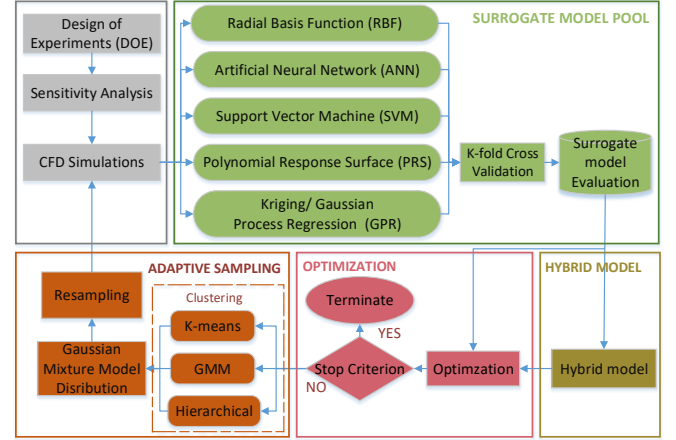


FIGURE 6: The framework of optimization and resampling

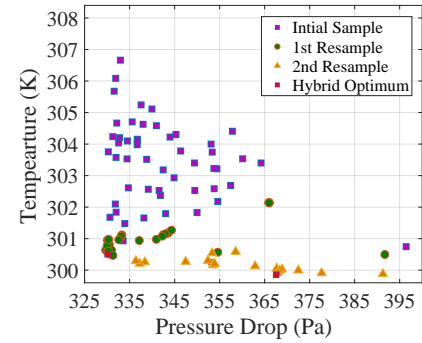


FIGURE 7: The optimization and resampling results

size, the optimal  $J$ -type BTMS has a 35.3% reduction in temperature rise, and a 63.4% improvement in temperature uniformity with a cost of 7.5% augment in pressure drop. The CFD simulation result of the optimal  $J$ -type BTMS design is illustrated in Fig. 8. It shows a small temperature standard deviation of 0.46 K. Though the structure optimization is performed under the benchmark working condition, this optimal structure is also able to uniformize the temperature distribution to some extent under dynamic working conditions, by adaptively controlling the opening degree of the two valves and the air mass flow rate. When the temperature difference between the left section and the right section accumulates to a certain level, the two control valves will change their opening degrees to shift the current cooling mode to another appropriate operation mode.

## 4 ARTIFICIAL NEURAL NETWORK BASED MODEL PREDICTIVE CONTROL

### 4.1 ANN Control Model Construction

As mentioned above, in order to prevent unnecessary operations of the two control valves, there are only three operation modes available for the  $J$ -type air-based BTMS, i.e.,  $J$ -mode,  $U$ -mode, and  $Z$ -mode, as illustrated in Fig.

**TABLE 2:** The optimal design of J-type BTMS

Parameter	$x_1$	$x_2$	$x_3$	$x_4$	$T_{max}$	$T_\sigma$	$\Delta P$
Unit	mm	mm	mm	mm	K	K	Pa
J-Benchmark	3	3	3	3	302.15	1.43	347.25
J-Optimized	2.8	2.7	2.2	2	299.98	0.46	391.28

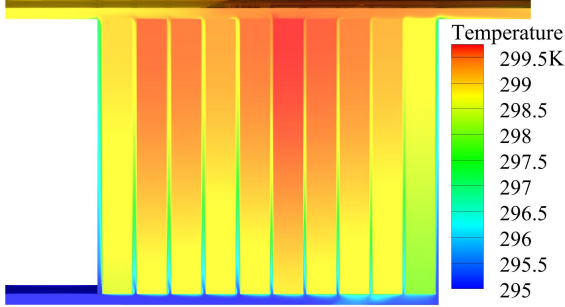


**FIGURE 8:** CFD simulation validation of the optimal J-type BTMS design

3. A total of 90 CFD simulations are conducted for every mode to characterize the relationship among the mass flow rate, battery temperature, and equivalent heat generation rate. Pressure drop is neglected here, though it is highly related to energy consumption and operating efficiency. Note that the simulations are set in transient mode with a time interval of 5 seconds, which makes the dynamic estimations of different parameters easier by dividing the continuous changing working conditions into discrete steady-state conditions of every 5 seconds and then integrating back to get the final results.

The battery temperature predictor is modeled via surrogate modeling with five inputs, which are the current stage: (i) the maximum temperature at the left side of battery module  $T_{left_k}$ , (ii) the maximum temperature at the right side of the battery module  $T_{right_k}$ , (iii) operation mode  $M_k$ , (iv) mass flow rate  $\dot{m}_k$ , and (v) heat generation rate  $\dot{Q}_k$ . There are three outputs of the surrogate model, i.e.,  $T_{left_{k+1}}$ ,  $T_{right_{k+1}}$ , and  $\dot{m}_{k+1}$ , which are the left side maximum temperature, the right side maximum temperature, and the operation mode of the next stage, respectively, as shown in Fig. 9. The operation mode is designed to switch from one to another when the temperature difference of the battery module exceeds 1 K as given by:

$$\begin{aligned} \text{If } T_{ref} - T_{right} > 1 K, & \text{ then switch to } U\text{-mode} \\ \text{If } T_{right} - T_{left} > 1 K, & \text{ then switch to } Z\text{-mode} \end{aligned} \quad (9)$$

By continuously controlling the operation mode, the temperature difference of the battery module is expected to be fully constrained within a reasonable range. Due to the highly nonlinear nature of the BTMS model, linearized PID control or fuzzy logic control may lose their accuracies under changing control conditions [23]. In this study, an ANN model is employed to establish the control system with a feed-forward structure and two hidden layers. The NRMSE of the ANN model is 11% by cross-validation. Moreover, given the appropriate discharging rate and its corresponding heat generation rate, the mass flow rate is constrained within 0.012 kg/s.

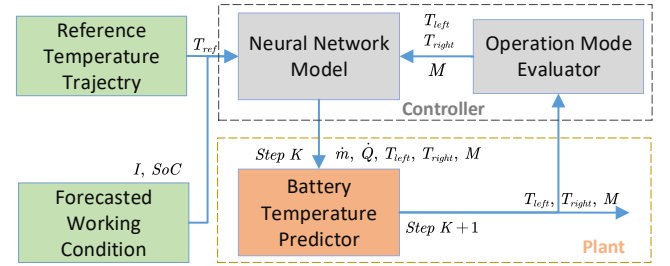


**FIGURE 9:** The architecture of the ANN controller

## 4.2 Case Study of ANN Control

Ideally, BTMS as well as battery management system should be controlled adaptively according to driving situations, which could be forecasted based on the driver's personal driving habits and vehicle stream, or transmitted directly from the autopilot system. In this study, the EPA Urban Dynamometer Driving Schedule (UDDS) illustrated in Fig. 10(a) is directly applied to test the thermal management system along with the ANN control strategy. The battery system of the EV consists of 8 series in parallel, and every series has 100 battery cells. The nominal voltage is as high as 375 V.

For a moving vehicle, the equivalent traction power can be estimated using Eq. 10.

$$P = \frac{V}{1000\eta} [mg(\mu\cos\alpha + \sin\alpha) + \frac{1}{2}\rho A_f C_d V^2 + m \frac{dV}{dT}] \quad (10)$$

The vehicle parameters and UDDS driving conditions are tabulated in Table 3. Correspondingly, the power profile is shown in Fig. 10(b), where the negative power represents the portion that can be regenerated back into the battery system by a regenerative brake system. Note that the reversible heat is significantly less than the resistance heat, and the charging heat can also be estimated with the

**TABLE 3:** Specification and driving condition (TESLA Model 3)

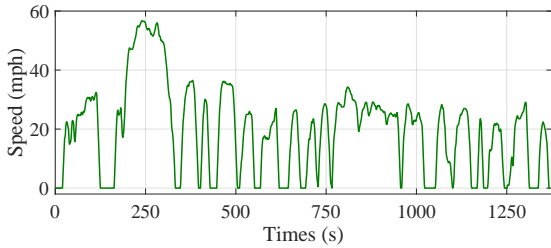
Mass	$m$	1,875 kg	Gradient	$\alpha$	0
Windward area	$A_f$	2.22 m <sup>2</sup>	Air friction Coeff	$C_d$	0.24
Standard gravity	$g$	9.8 m/s <sup>2</sup>	Motion efficiency	$\eta$	0.98
Air density	$\rho$	1.16 kg/m <sup>3</sup>	Rolling resistance	$\mu$	0.01
Velocity	$V$	-	Regenerative Coeff	$\eta_r$	0.8

electro-thermal model. The equivalent current and the SoC are shown in Fig. 10(c). In this study, the SoC is defined using the Coulomb counting method, as given by:

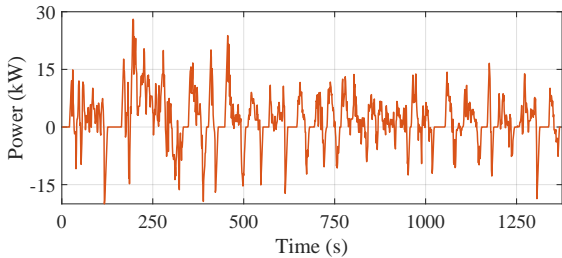
$$SoC = SoC_{init} - \frac{\int i dt}{Q} \quad (11)$$

where  $SoC_{init}$  and  $Q$  denote the SoC of the initial stage and the battery capacity, respectively.

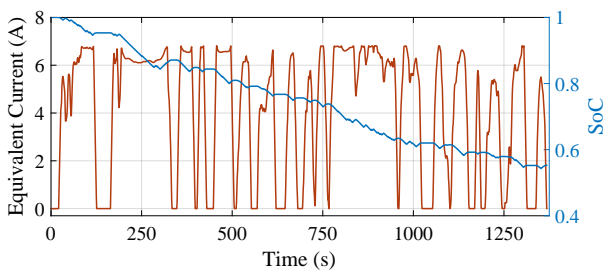
A reference temperature with two portions is predefined based on the UDDS driving cycle: a climbing section that has a temperature rise of 6 K in 20 minutes, and a stationary section of 309 K for the rest of the cycle time. All these parameters are imported into the ANN control system, as shown in Fig. 11. Figure 11(a) shows that the BMTS starts with  $J$ -mode, where the left side temperature  $T_{ref}$  is dominating. The temperature difference reaches the tipping point in about 11 minutes, and the operation mode switches from  $J$ -mode to  $U$ -mode. Most of the air flows out of the package from the  $U$ -valve, which lowers the battery temperature of the left side and prevents a larger temperature difference. As presented in Fig. 11(b), the mass flow rate is able to adaptively follow the dynamic inputs of heat generation rate under varying working conditions. The results also suggest that the air cooling is capable of dealing with light-duty daily driving cycles like UDDS.



(a) The profile of velocity

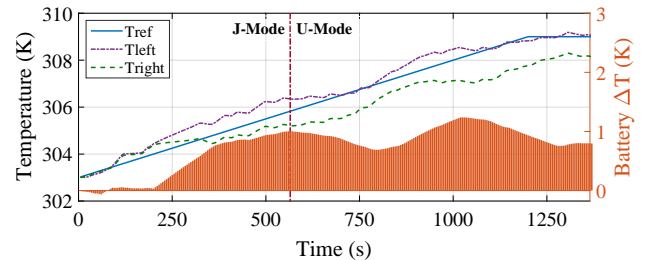


(b) The profile of power

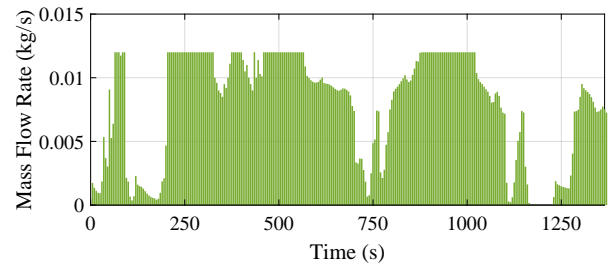


(c) The profile of equivalent current and SoC

**FIGURE 10:** Profiles of the UDDS driving cycle



(a) The profile of temperature



(b) The profile of air mass flow rate

**FIGURE 11:** ANN control profile of the UDDS driving cycle

### 4.3 Case Study of ANN-based MPC Strategy

Though the ANN controller is able to successfully control the battery temperature within a narrow range, it is recognized from Fig. 11(b) that the system fails to foresee the rapid increasing temperature, thus resulting in the full load running of the cooling system. As a sequence, the BTMS switches to *U*-mode that has a relatively lower cooling efficiency. To further improve the cooling efficiency, a MPC control strategy is integrated with the ANN system, as shown in Fig. 12.

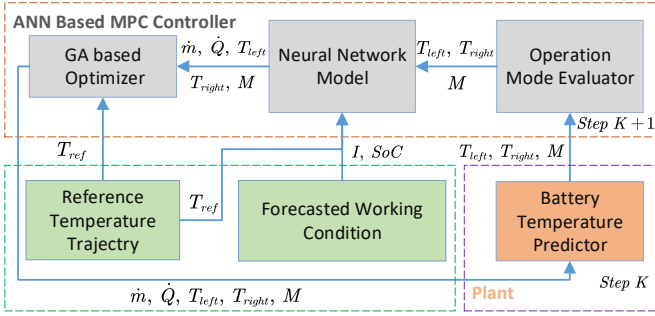


FIGURE 12: The architecture of ANN-based MPC strategy

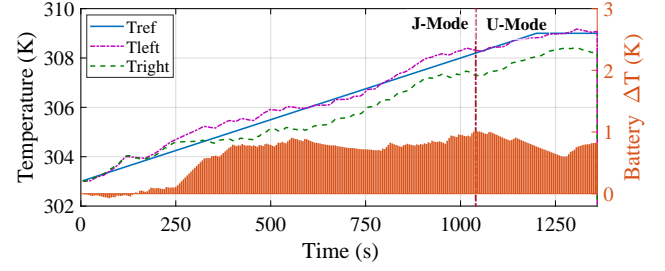
The genetic algorithm is adopted here to optimize the temperature difference between the reference temperature trajectory and the battery maximum temperature, as given by:

$$\arg \min_{\dot{m}} J = \sum_k^3 (T_{ref_k} - T_{max_k})^2 \quad (12)$$

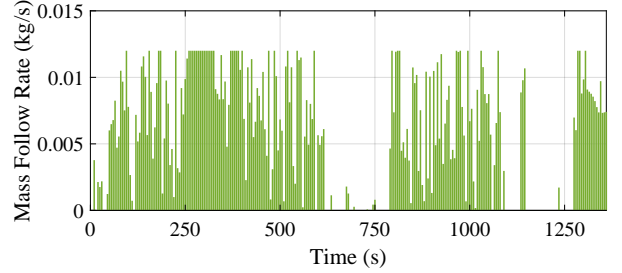
subject to  $0 \leq \dot{m} \leq 0.012$

where  $\dot{m}$  denotes the mass flow rate,  $T_{ref}$  is the reference temperature trajectory, and  $T_{max}$  is the maximum temperature of the battery module, defined as  $T_{max} = \max(T_{left}, T_{right})$ . The predictive horizon covers three samples, i.e., 15 seconds in total.

Figure 13 shows the temperature and mass flow rate profiles of the ANN-based MPC strategy. By forecasting the forthcoming load, the control system is able to lower the temperature in advance and provide more control capacity to the system. Compared with the mass flow rate with the ANN control, the ANN-based MPC strategy is more effective, especially in the range between 100 s and 250 s. The NRMSE between the maximum battery temperature and the reference temperature under the ANN-based MPC strategy is  $8.5E-4 K$  compared to  $1.3E-3 K$



(a) The profile of temperature



(b) The profile of air mass flow rate

FIGURE 13: ANN-based MPC profile of the UDDS driving cycle

of the ANN control, as illustrated in Fig. 14. It also suggests that the overall temperature difference between the left part and right part of battery module under the ANN-based MPC strategy is much smaller than that of the ANN control case. From the perspective of energy efficiency, we also observe is that the air consumption under ANN-based MPC is much less than that under the ANN control due to different cooling efficiency. Overall, the developed self-adapting intelligent *J*-type BTMS via ANN-based MPC is capable of controlling the temperature rise as well as the temperature uniformity in a reasonable range.

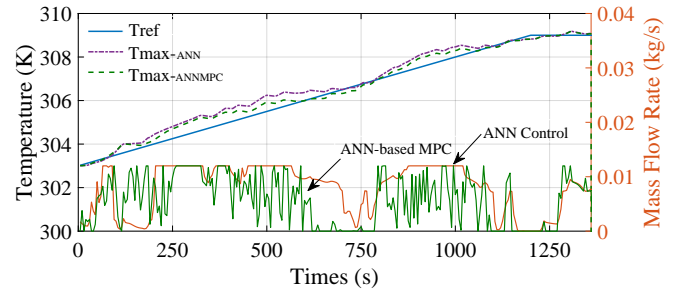


FIGURE 14: A comparison between ANN control and ANN-based MPC strategy

## 5 CONCLUSION

This paper developed a self-adapting air-based  $J$ -type battery thermal management system. Based on the newly-established electro-thermal model, surrogate-based optimization was first performed to optimize the structure of the  $J$ -type BTMS. Results showed that the optimized  $J$ -type BTMS has a 35.3% reduction in temperature rise, and a 63.4% improvement in temperature uniformity, with a cost of 7.5% augment in pressure drop compared to the benchmark case.

Based on the optimized  $J$ -type BTMS, an ANN-based MPC model was developed and tested with the UDDS driving cycle. Results showed that the mass flow rate and BTMS operation mode could be adaptively controlled under dynamic working conditions, and the battery temperature difference could be constrained within a narrow range. We also found that the ANN-based MPC strategy performed better than the ANN controller, thereby improving the overall BTMS cooling efficiency. Potential future work will integrate the self-adapting  $J$ -type battery thermal system together with the operations of other equipments like air conditioner for an optimal battery discharging scheduling.

## 6 ACKNOWLEDGMENTS

The authors would like to thank Prof. Babak Fahimi and Dr. Zhuo Yang, at the Department of Electrical and Computer Engineering, The University of Texas at Dallas, for providing data on battery electro-thermal modeling.

## REFERENCES

- [1] Pesaran, A., Santhanagopalan, S., and Kim, G., 2013. Addressing the impact of temperature extremes on large format li-ion batteries for vehicle applications (presentation). Tech. rep., National Renewable Energy Lab.(NREL), Golden, CO (United States).
- [2] Ramadass, P., Haran, B., White, R., and Popov, B. N., 2002. "Capacity fade of sony 18650 cells cycled at elevated temperatures: Part i. cycling performance". *Journal of Power Sources*, **112**(2), pp. 606–613.
- [3] Park, C., and Jaura, A. K., 2003. Dynamic thermal model of li-ion battery for predictive behavior in hybrid and fuel cell vehicles. Tech. rep., SAE Technical Paper.
- [4] Xia, G., Cao, L., and Bi, G., 2017. "A review on battery thermal management in electric vehicle application". *Journal of Power Sources*, **367**, pp. 90–105.
- [5] Grande, L., and He, X. Advanced li-ion beyond li-ion batteries 2018-2028. [Online] Available at: "https://www.idtechex.com/research/reports/advanced-li-ion-and-beyond-li-ion-batteries-2018-2028-000566.asp. [Accessed Jan 2018].
- [6] Li, M., Liu, Y., Wang, X., and Zhang, J., 2019. "Modeling and optimization of an enhanced battery thermal management system in electric vehicles". *Frontiers of Mechanical Engineering*, **14**(1), pp. 65–75.
- [7] Wang, X., Li, M., Liu, Y., Sun, W., Song, X., and Zhang, J., 2017. "Surrogate based multidisciplinary design optimization of lithium-ion battery thermal management system in electric vehicles". *Structural and Multidisciplinary Optimization*, **56**(6), pp. 1555–1570.
- [8] Xun, J., Liu, R., and Jiao, K., 2013. "Numerical and analytical modeling of lithium ion battery thermal behaviors with different cooling designs". *Journal of Power Sources*, **233**, pp. 47–61.
- [9] Park, H., 2013. "A design of air flow configuration for cooling lithium ion battery in hybrid electric vehicles". *Journal of power sources*, **239**, pp. 30–36.
- [10] Kim, J., Oh, J., and Lee, H., 2018. "Review on battery thermal management system for electric vehicles". *Applied Thermal Engineering*.
- [11] Shahid, S., and Agelin-Chaab, M., 2017. "Analysis of cooling effectiveness and temperature uniformity in a battery pack for cylindrical batteries". *Energies*, **10**(8), p. 1157.
- [12] He, F., and Ma, L., 2015. "Thermal management of batteries employing active temperature control and reciprocating cooling flow". *International journal of heat and mass transfer*, **83**, pp. 164–172.
- [13] Gao, X., Ma, Y., and Chen, H., 2018. "Active thermal control of a battery pack under elevated temperatures". *IFAC-PapersOnLine*, **51**(31), pp. 262–267.
- [14] Tao, X., and Wagner, J., 2016. "A thermal management system for the battery pack of a hybrid electric vehicle: modeling and control". *Proceedings of the Institution of Mechanical Engineers, Part D: Journal of Automobile Engineering*, **230**(2), pp. 190–201.
- [15] Liu, Y., Ghassemi, P., Chowdhury, S., and Zhang, J., 2018. "Surrogate based multi-objective optimization of j-type battery thermal management system". In ASME 2018 International Design Engineering Technical Conferences and Computers and Information in Engineering Conference, American Society of Mechanical Engineers, pp. V02BT03A034–V02BT03A034.
- [16] Cheng, X.-B., Zhang, R., Zhao, C.-Z., and Zhang, Q., 2017. "Toward safe lithium metal anode in rechargeable batteries: a review". *Chemical reviews*, **117**(15), pp. 10403–10473.
- [17] Rao, L., and Newman, J., 1997. "Heat-generation rate and general energy balance for insertion battery systems". *Journal of the Electrochemical Society*, **144**(8), pp. 2697–2704.
- [18] Yang, Z., Patil, D., and Fahimi, B., 2018. "Online estimation of capacity fade and power fade of lithium-ion

- batteries based on input–output response technique”. *IEEE Transactions on Transportation Electrification*, **4**(1), pp. 147–156.
- [19] Yang, Z., Patil, D., and Fahimi, B., 2019. “Electrothermal modeling of lithium-ion batteries for electric vehicles”. *IEEE Transactions on Vehicular Technology*, **68**(1), pp. 170–179.
- [20] Lophaven, S., Nielsen, H., and Sondergaard, J., 2016. Dace a matlab kriging toolbox [eb/ol].
- [21] Zhang, J., Chowdhury, S., and Messac, A., 2012. “An adaptive hybrid surrogate model”. *Structural and Multidisciplinary Optimization*, **46**(2), pp. 223–238.
- [22] Song, X., Lv, L., Li, J., Sun, W., and Zhang, J., 2018. “An advanced and robust ensemble surrogate model: Extended adaptive hybrid functions”. *Journal of Mechanical Design*, **140**(4), p. 041402.
- [23] Yan, J., Xu, G., Qian, H., and Xu, Y., 2010. “Battery fast charging strategy based on model predictive control”. In 2010 IEEE 72nd Vehicular Technology Conference-Fall, IEEE, pp. 1–8.